

EXPERIMENTAL ANALYSIS OF HOMEOSTATIC-INSPIRED MOTION CONTROLLER FOR A HYBRID-DRIVEN AUTONOMOUS UNDERWATER GLIDER

Khalid Isa^{a*}, M. R. Arshad^b

^aEmbedded Computing System Research Focus Group (EmbCoS), Department of Computer Engineering, Faculty of Electrical and Electronic Engineering, Universiti Tun Hussein Onn Malaysia (UTHM), 86400 Parit Raja, Batu Pahat, Johor, Malaysia

^bUnderwater Control and Robotics Group (UCRG), School of Electrical and Electronic Engineering, Engineering Campus, Universiti Sains Malaysia(USM), 14300 Nibong Tebal, Pulau Pinang, Malaysia

Article history

Received

13 March 2015

Received in revised form

14 April 2015

Accepted

15 June 2015

*Corresponding author
halid@uthm.edu.my

Graphical abstract



Abstract

This paper presents a homeostatic controller algorithm and its performance, which controls motion of a hybrid-driven underwater glider. The homeostatic controller is inspired from a biological process known as homeostasis, which maintains a stable state in the face of massively dynamics conditions. The objective is to obtain a better control performance of the glider motion control system with a presence of disturbance, which is the water current. The algorithm was simulated by using MatlabTM. According to the simulation results, in order to achieve the desired pitch angle, the homeostatic controller was able to optimize the glider's ballast mass and distance of the glider's sliding mass by reducing the ballast mass up to 17.7% and shortening the sliding mass distance up to 53.7% when compared with the linear-quadratic regulator (LQR) and model predictive control (MPC). Furthermore, validation analyses of the homeostatic controller performance between the simulation and experimental results have shown very satisfactory performance.

Keywords: Homeostatic controller, hybrid-driven underwater glider, homeostasis, motion control

Abstrak

Kertas kerja ini membentangkan algoritma pengawal homeostatic dan pencapaiannya, yang mengawal gerakan gelungsur air hybrid. Pengawal homeostatic diilhamkan daripada proses biologi homeostasis yang mengekalkan keadaan stabil pada keadaan dinamik yang besar. Objektifnya ialah untuk mendapatkan pencapaian kawalan yang lebih baik pada gelungsur air dengan kehadiran gangguan, iaitu gelombang air. Algoritma ini telah disimulasikan menggunakan MatlabTM. Berdasarkan kepada hasil simulasi, untuk mendapatkan sudut satah yang diinginkan, pengawal homeostatik berkebolehan untuk mengoptimalkan jisim balast gelungsur dan jarak antara masa gelungsur dengan mengurangkan jisim balast sebanyak 17.7% dan memendekkan jarak gelungsur sehingga 53.7% jika dibandingkan dengan Linear Quadratic Regulator (LQR) dan Model Predictive Control (MPC). Tambahan pula, analisis kesahan pencapaian pengawal homeostatik antara simulasi dan hasil eksperimen menunjukkan pencapaian yang memuaskan.

Kata kunci: Pengawal homeostatic, gelungsur air hybrid, homeostasis

© 2015 Penerbit UTM Press. All rights reserved

1.0 INTRODUCTION

An autonomous hybrid-driven glider is a new breed of autonomous underwater glider, which integrates the concept of a buoyancy-driven underwater glider and a conventional autonomous underwater vehicle (AUV). The USM hybrid-driven underwater glider was developed in order to overcome the speed and manoeuvrability limitations of the buoyancy-driven underwater glider. Most existing underwater gliders such as Slocum [1], Spray [2], Seaglider [3] and Deepglider [4] are the buoyancy-driven glider. These gliders were designed to fulfil the demand of a low energy consumption underwater vehicle, which can be used for long-term oceanographic sampling [1-5]. However, typical buoyancy-driven gliders are considered an under-actuated system, relatively slow, have limited external moving surfaces, and have major constraints for manoeuvring and control. Thus, the development of the USM hybrid-driven AUG could increase the glider's speed and manoeuvrability. However, the design complexity will likely necessitate energy consumption increases. This challenge can be addressed by managing the driving system of the glider efficiently.

In terms of glider controller, most existing gliders used the PID and LQR controller to control the motion and attitude [6-11]. The sliding mode control (SMC) has also been used to control the glider [12-13], but the main constraint in SMC is the chattering effect, which can degrade the performance of the system, and make the system unstable. Although these controller methods have demonstrated acceptable results, these control methods still face difficulties in tuning the controller gains to maintain overall stability and high-quality response when the control performance degrades due to significant changes in the vehicle dynamics and its environment. The high nonlinearity and time-variance of underwater vehicle dynamics, and unpredictable underwater disturbances such as the fluctuating water currents are the main reasons that make the underwater vehicles such as the underwater glider difficult to control [14-16]. Thus, it is highly desirable to design a controller that has a self-tuning and an adaptive ability to deal with these constraints.

Due to that, the glider should be truly autonomous which operate steadily and adaptively to their environment. Therefore, biologically inspired control systems should be considered because they are autonomous and adaptive in nature. One possible approach comes from a biology process, which known as homeostasis. This biological process has inspired and motivated applications of homeostasis in the synthesis of autonomous systems in mobile robotics as presented in [17-18]. However, until now, the effectiveness of the homeostatic controller on an underwater platform such as the AUV or glider has not been investigated. Due to that, the homeostatic controller algorithm for glider motion control has been designed and developed in this research work.

2.0 THE HYBRID-DRIVEN UNDERWATER GLIDER MODEL AND PROTOTYPE

The 3D model of the glider was designed by using CAD software, namely Solidworks TM. The drawing process was accomplished by drawing separately all of the main glider's structures and parts for fabrication. Then, all of these parts were assembled together to form a complete 3D model of the glider. Figure 1 shows the 3D model of the glider.

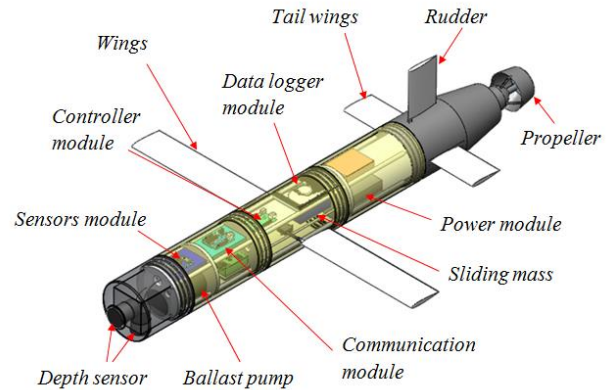


Figure 1 3D model of the hybrid-driven underwater glider

Technically, the hybrid-driven autonomous underwater glider is composed of a cylindrical hull with a nose and tail, a propeller, a controllable rudder, controllable wings, an internal sliding mass, ballast pump, controller module, antenna module and power module. The internal sliding mass and ballast pump are known as the internal actuators. These actuators control the pitch angle and buoyancy, respectively. In contrast, the controllable wings and the rudder, which are known as the external actuators, control the manoeuvrability (roll and yaw angle) of the glider. Thus, the glider can be propelled by using buoyancy or the propeller as well as by using both propulsion systems at the same time. Figures 2 and 3 show the glider exterior and interior configurations, respectively.

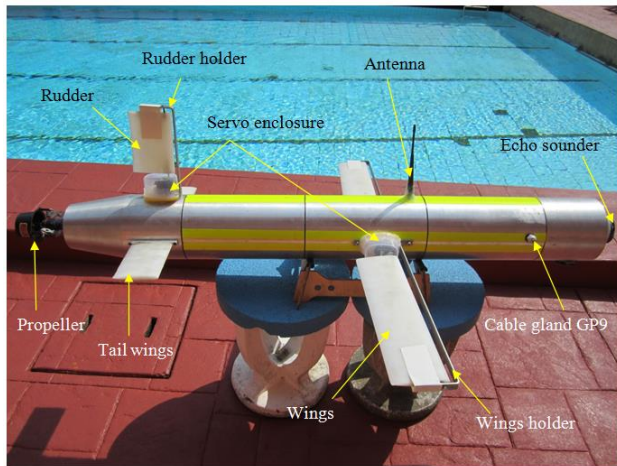


Figure 2 Exterior configuration of the hybrid-driven underwater glider

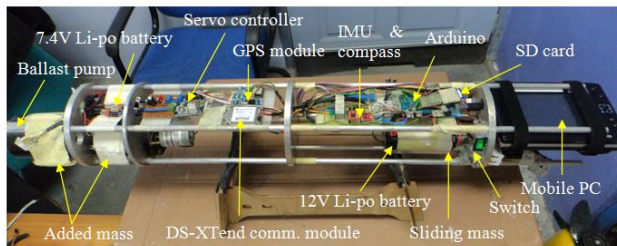


Figure 3 Interior configuration of the hybrid-driven underwater glider

In order to model this glider mathematically, a coupled model has been derived and presented extensively in Isa *et al.* [19]. The glider has been mathematically modelled based on the Newton-Euler approach and the presence of water currents as a disturbance being taken into account. In addition, the hydrodynamics of the hybrid-driven AUG have been estimated by using two methods: an analytical method based on Strip theory and computational fluid dynamic method (CFD). The Strip theory analysis was simulated by MATLABM, while FluentTM and GambitTM were used to simulate the CFD. The purpose of using these methods is to compare and analyze the accuracy of the estimated coefficient values of the glider hydrodynamics. Then, the model was simulated by using MATLABM in order to analyze the glider stability and controllability in an open-loop system.

The basic measurement and setting are based on the Slocum design [1]. However, a modular design was implemented for the glider hull, which means that the glider hull was divided into three smaller hulls instead of designing one long hull. The length of each hull was 300 mm, which made the total length of the hull 900 mm. On the hand, the length of the nose and tail were 215 mm and 385 mm, respectively. However, the overall length of the glider, with an additional length from the propeller located at the tail and echo sounder located at the nose, was 1650 mm. The diameter of the glider was 170 mm. Each of these parts has a screw thread and

O-ring to make it easier to assemble and to ensure that the glider was watertight. The total weight of the glider was 30.95 kg.

The wings, tail wings and rudder were designed based on the National Advisory Committee for Aeronautics (NACA) 0012 airfoils. Although the NACA airfoil series is normally used for designing the wings of airplanes, it can be implemented in the design of a glider's wings and glider's rudder due to the similar concept of the gliding motion. The width of the wings and rudder was 0.1 m. The wings and the rudder were modelled as controllable actuators, and the tail wings were modelled as fixed components for stabilising the glider.

3.0 HOMEOSTATIC CONTROLLER ALGORITHM

Homeostatic control is a control mechanism of the homeostasis process in human or mammal bodies that is responsible for maintaining physiological or biological systems. Biologically, homeostatic control consists of three major components: the nervous system, endocrine system and immune system. Thus, an artificial controller is the artificial counterpart of these biological systems, which are represented as: artificial neural networks (ANNs), artificial endocrine system (AES) and artificial immune system (AIS). The homeostatic control mechanism has inspired and motivated numerous research works such as Di Paolo [20], Hoinville and Henaff [21], Vargas *et al.* [22], Moiola *et al.* [23] and [24], Neal and Timmis [25] and Timmis *et al.* [26]. However, no previous research work in the robotics and control area has examined the idea of introducing a controller algorithm by integrating the neural-endocrine-immune system. Figure 4 shows the homeostatic control system framework for the glider.

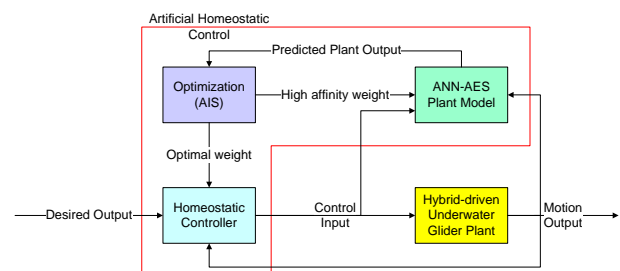


Figure 4 The artificial homeostatic control framework of the glider motion

Biologically, homeostatic control consists of three major components: the nervous system, endocrine system, and immune system. Thus, an artificial homeostatic controller is the artificial counterpart of these biological systems, which are represented as: artificial neural networks (ANNs), artificial endocrine system (AES) and artificial immune system (AIS).

3.1 Artificial Neural Network (ANN)

The ANN fulfils the same role as that played by the natural nervous system; it is connected to both the sensor units and actuators of the glider system. The ANN is designed to link a number of neurons that represent the control inputs and outputs of the glider plant. The neural networks (NN) control method has been applied to the underwater vehicles because of its robustness and adaptability to the high nonlinearity and dynamic environment of the vehicle. Furthermore, neural networks are able to handle multivariable control problems of Multiple-Input-Multiple-Output (MIMO) systems, such as the hybrid-driven AUG with low rates of control update.

In this work, the ANN controller based on predictive control method has been designed to predict the control inputs and outputs for the glider in order to achieve the desired output for certain types of motion. The controller required two models of the glider: the forward model (ANN glider plant model) and the inverse model (ANN controller). These models have been designed by using multilayer perceptron (MLP) network architecture. The forward model is designed to represent the glider plant. Before the glider plant was modelled, the nonlinear glider plant was linearized about an initial operating point to obtain the state-space representation of the MIMO system of the hybrid-driven glider.

Initially, the open loop system of the nonlinear glider plant model has 10 inputs, 17 states, and 17 outputs. The inputs are the deflection angle of wings and a rudder (δ_{rw}, δ_{lw} and δ_r), the net forces of a sliding mass (u_x and u_z), ballast pumping rate (u_b), propeller force (τ_{PX}), and the water current velocities (u_r, v_r, w_r). The states and outputs are the glider position (x, y and z), the Euler angles (ϕ, θ and ψ), the glider velocities (u, v and w), the glider accelerations (p, q and r), the sliding mass positions (r_{px} and r_{pz}), the sliding mass forces (p_{px} and p_{pz}), and the ballast mass (m_b). However, after the initialization, only the first six inputs were selected as the parameters of interest for the motion control system analysis.

The forward model of the glider plant consists of a three-layer network with 6 input nodes as the control inputs, 6 hidden layer nodes, and 14 output nodes to control the glider motion and attitude. The input of the network is a matrix B from the state-space matrices, and the output is a matrix A. The number of hidden nodes is determined based on 5 trials with different number of nodes, which were 2, 4, 6, 8 and 10 hidden layer nodes. As a result, the 6 hidden layer nodes produced the best results, whereas the 2 and 4 hidden layers were not able to stabilise the glider model, and the 8 and 10 hidden layers did not produced better performance.

Then, this model is trained by the backpropagation training algorithm in order to predict the plant outputs. In this work, gradient descent with momentum and adaptive learning rate backpropagation is implemented as the

backpropagation training algorithm. In addition, the log-sigmoid transfer function is used in the hidden layer and output layer. Figure 5 shows the ANN glider plant model.

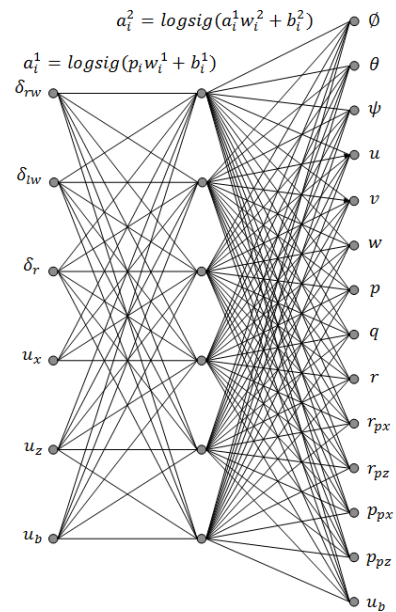


Figure 5 The ANN forward model of the glider plant

The activation function of the neuron in the hidden layer is defined as:

$$a_i^1 = \text{logsig}(p_i w_i^1 + b_i^1), \tag{1}$$

and the activation function of the neuron in the output layer is defined as:

$$a_i^2 = \text{logsig}(a_i^1 w_i^2 + b_i^2), \tag{2}$$

where p_i is the input node value, w_i is the weight and b_i is the bias of the network. However, the Equation (2) will be rewritten when the AES is introduced as the weight tuner in the output layer of the network. This new equation defines the new activation function that depends on the hormone concentration and the sensitivity of the neuron to the hormone.

On the other hand, the inverse model of the glider plant predicts the control inputs for the glider. It is also known as the neural network controller. This controller response is presented in a discrete time domain, which is based on the receding horizon method [27]. Thus, the time-invariant discrete time system dynamics of the glider based on predictive control concepts are defined as [28]:

$$x(k+1) = A_d x(k) + B_d u(k), \tag{3}$$

$$y(k) = C_d x(k), \tag{4}$$

$$z(k) = C_z x(k), \tag{5}$$

where $k=0,1,2,3,\dots$, $x(k)$ is the discrete states, A_d is the desired state matrix A from the state-space representation, B_d represents the desired input matrix B , $u(k)$ is the control inputs, $y(k)$ is the system outputs, C_d represents the output matrix C , $z(k)$ is the controlled outputs, and C_z represents the controlled output matrix.

The control inputs were selected by an optimization process over a specified time horizon, t , prediction horizon, P , and control horizon, M . In this work, the value of sampling time (time horizon), prediction horizon and control horizon have been determined as equal to 1, 15 and 5, respectively. The neural network controller optimizer, based on a numerical optimizer (also known as the quadratic programming solver), computes the sequence of present and future control actions in order to achieve the desired outputs. In addition, the controller also minimizes the cost function in order to obtain optimum control input. Thus, the cost function is defined in quadratic form as:

$$J = \sum_{k=P_1}^P [y(t+k) - y_d(t+k)]^2 + \lambda \sum_{k=1}^M [u(t+k-1) - u(t+k-2)]^2, \quad (6)$$

where P_1 is the minimum prediction horizon, y_d represents the desired outputs, u' is the tentative control signal, λ represents the weight factor, and the constraints are defined as:

$$y_{\min} \leq y(t+k) \leq y_{\max}, k = 1, \dots, P, \quad (7)$$

$$u_{\min} \leq u(t+k) \leq u_{\max}, k = 0, \dots, M-1, \quad (8)$$

$$|\Delta u(t+k)| \leq u_{\max}, k = 0, \dots, M-1, \quad (9)$$

$$|\Delta u(t+k)| = 0, k = M, \dots, P-1. \quad (10)$$

3.2 Artificial Endocrine System (AES)

In line with the biological mechanism, the AES has these two major components: glands and hormones. The artificial hormones will be secreted into the ANN by the artificial gland, g , when the gland is stimulated by certain factors (either external or internal stimuli). This means that this artificial hormone can only affect the neurons based on certain conditions. Thus, in this work, the artificial gland will be triggered to release the hormone when the sensitivity of the ANN's weight in the output layer is lower than zero ($w_i^2 < 0$) or the disturbance from the water currents is greater than zero ($V_c > 0$). In biological endocrine systems, a neuron can be affected by several hormones, and not every hormone must affect every neuron [29]; which neurons are affected depends on the sensitivity of the neuron to the hormone, S_{ig} . However, in this work, every neuron is assumed to be

affected by one hormone with a constant value of the S_{ig} . In addition, there are two main functions in the secretion of the artificial endocrine gland: the gland stimulation rate, S_{rg} , and the hormone concentration, G_{cg} . Thus, referring to Timmis *et al.* [29], the stimulation rate of the gland is denoted as R_g , which is defined as:

$$R_g(t) = \alpha_g \sum_i A_i(t), \quad (11)$$

where α_g is the hormone stimulation rate, and A_i is the sensor inputs signal.

However, in this work, the A_i has been replaced by the matrix A of the state-space representation of the neural network plant model, A_n . In addition, the stimulation rate of the gland is defined by taking the current concentration of hormone, $G_{cg}(t)$, into account. Thus, the stimulation rate of the gland in Equation 11 is redefined as:

$$S_{rg}(t) = \frac{\alpha_g}{1 + G_{cg}(t)} A_n(t), \quad (12)$$

and the hormone concentration, G_{cg} , is defined as:

$$G_{cg}(t) = \beta_g G_{cg}(t) + S_{rg}(t), \quad (13)$$

where β_g is the decay rate of the hormone.

The function of the decay rate is to reduce the concentration of the hormone gradually. In this work, the value of hormone stimulation rate, α_g , and decay rate, β_g , is between the value of 0 and 1. These parameters are crucial because they influence the behaviour response of the glider. The hormone stimulation rate indicates the quantity of hormone released by the gland. On the other hand, the decay rate indicates the duration for which hormones remain in the system. Thus, from the formulation above, the activation function for the gland is defined as:

$$a_g = \text{logsig}(G_{cg} S_{ig}), \quad (14)$$

where the value of S_{ig} is between 0 and 1. In this work, the ideal value of hormone stimulation rate, α_g , decay rate, β_g , and sensitivity of the neuron to the hormone, S_{ig} , based on Timmis [27], were determined to be 0.9, 0.4 and 0.01, respectively.

Then, by multiplication of the activation function of the gland with the weight of the ANN, the activation function of the network (i.e. neuroendocrine network) is defined as:

$$a_{ne} = \text{logsig}(p_i w_i G_{cg} S_{ig} + b). \quad (15)$$

This activation is simulated when the sensitivity of the ANN's weight in the output layer is negative or disturbance from the water current occurs. The sensitivity of the output layer weight is determined by using the sensitivity function provided by MATLABM. This function computes the performance index or cost function, J , and the derivatives for each output

layer node with respect to the output weights. Therefore, by tuning the controller weights through the AES, the control system is able to compensate the disturbance as well as to increase the control performance by reducing the cost function of the control system. Thus, the activation function of the neuron in the output layer in the Equation 2 is rewritten as:

$$a_i^2 = \text{logsig}(a_i^1 w_i^2 G_{cg} S_{ig} + b_i^2). \quad (16)$$

3.3 Artificial Immune System (AES)

The AIS can be utilized in two approaches. Firstly, as a regulator for cell growth by removing cells, neurons, glands or connections that have a detrimental impact on the system functionality. Secondly, as an optimizer of responses to the disturbances which could be environmental changes that affect the system. In this work, the latter approach has been selected in order to optimize the weights of the neuroendocrine network. Thus, the AIS based on CSA has been designed to optimize the controller weight to obtain better control performance.

Biologically, the natural immune system used the clonal selection to define the basic response of the immune system to an antigenic stimulus. The idea of this theory is to proliferate the cells only if the cells able to recognize the antigens (Ag). As an example, when a human is exposed to an antigen, the B lymphocyte cell in a human's body responds by producing antibodies (Ab). Each cell releases only one antibody specifically to an antigen. Then, the antigen attached to the antibody and with the signal from the T-helper cell, the antigen stimulates the B cell to proliferate and mature into plasma cells.

Initially, the clonal selection algorithm (CLONALG) by De Castro and Von Zuben [30] is proposed to solve the pattern recognition problem. In this work, there are two populations that need to be characterized in the clonal selection algorithm (CSA): a population of antigens (Ag), and a population of antibodies (Ab). The Ab population is a set of current candidate solutions, and Ag is the set of weights to be recognized. Thus, the Ab population is randomly initialized based on the number of weights, Ag. After the initialization of the first population, the looping condition is determined based on a predefined maximum number of generations. In the algorithm, the first step of the looping process is to determine the fitness function (affinity) values of all antibodies (Ab). Then, the cloning process selects antibodies with high affinity values (best Ab) so that they can be cloned independently. The selected Ab should be cloned proportionally to their Ag affinities in order to generate the clone population. Then, the affinity maturation process is carried out by the mutation operator in order to generate the matured clone population. The mature rate of the clone population is defined as:

$$m_r = e^{-f}, \quad (17)$$

where e is the exponential and f is the fitness function value of best Ab population that has been normalized. Lastly, the algorithm randomly creates new Ab for replacing the lowest-affinity Ab.

Thus, the CSA in this work is designed to evolve the weight of the neuroendocrine network by means of selection, cloning, mutation and editing processes. Following is the process of the AIS:

- a) Initialization: Randomly initializes a population of the antibodies (Ab) based on the number of weights/antigens (Ag).
- b) Evaluation: Compute all the affinity values for the Ab.
- c) Selection and Cloning: Select the Ab with the highest affinity value and generate the clones of the Ab proportionally to their affinity with the Ag.
- d) Mutation: Mutate the clones inversely proportionally to their affinity. Then, add these clones to the set of Ab and place a copy of the matured Ab into the memory set.
- e) Editing: Replace the lowest-affinity Ab with a new randomly-generated Ab.
- f) Repeat: Repeat the process until the optimal weight is achieved or the looping condition is met.

3.4 Artificial Homeostatic Controller Algorithm

The artificial homeostatic controller algorithm for the hybrid-driven AUG is presented in Figure 6. The algorithm starts by initializing the parameters of the glider structure and configuration, control inputs, and control outputs. Then, the linearization process of the open-loop system of the nonlinear glider plant model is performed in order to obtain the state-space representation of the glider model. In this work, the linearization process was carried out by using the linmod function provided by MATLABM, which is based on the Jacobian linearization method. Subsequently, set the desired outputs of the glider plant and the running time of the system. In the simulation and experiment, the Euler angles of the glider were used as the desired outputs for the control system because the glider prototype used the IMU sensors and compass as the sensors.

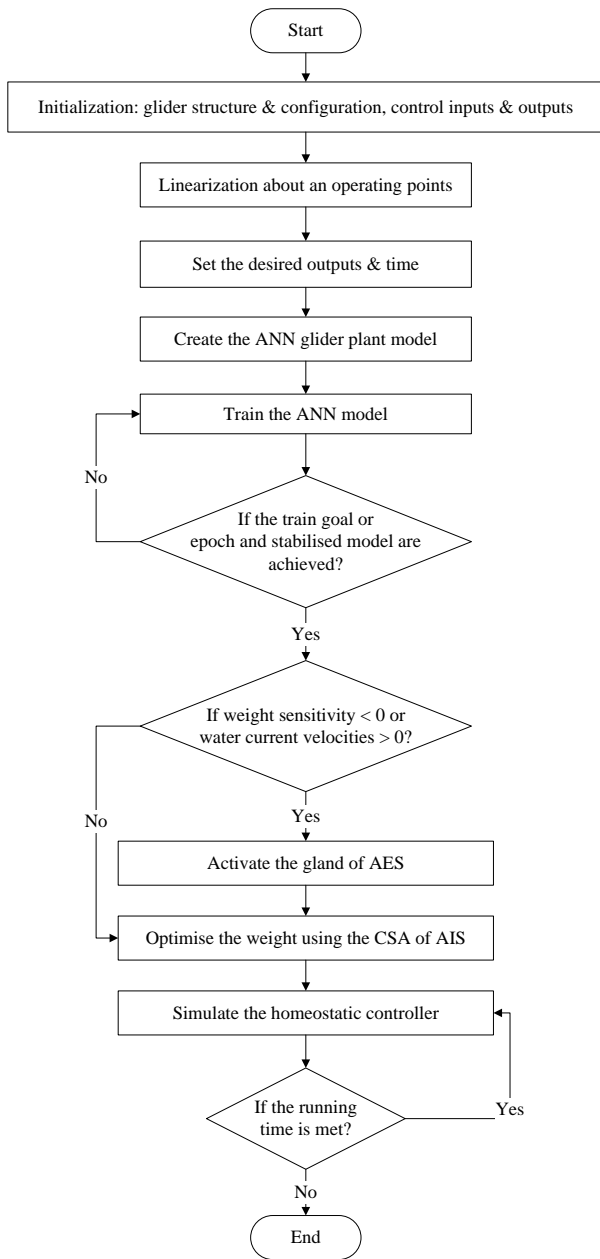


Figure 6 The homeostatic controller algorithm

4.0 RESULTS AND ANALYSES

The homeostatic controller performance was compared with the performance of the LQR, MPC, NN, and neuroendocrine controllers. Thus, the straight gliding motion was simulated for benchmarking the performance of the homeostatic controller over these controller methods. For the experimental results, two tests were conducted at the USM diving pool: open-loop and closed-loop tests. Three types of motion were tested: the propeller-driven, buoyancy-driven and hybrid-driven. However, in this paper, only the results and analyses of hybrid-driven mode test are presented.

4.1 Benchmarking of Homeostatic Controller Performance over Other Controller Methods

In this simulation, the system with disturbance, where the velocities of the water currents as the disturbance were assumed as 0.5 m/s, was simulated for 120 seconds, with 30-second duration for each angle. Table 1 shows the desired outputs for the simulation of all controller methods.

Figures 7 and 8 show the benchmarking results of the homeostatic controller performance over the LQR, MPC, neural network, and neuroendocrine controllers. Figure 7 shows that all the controllers achieved the desired pitch angle. Although only prominent lines were visible in the graphs, the results show that the performance of the neuroendocrine controller was somewhat similar to that of the homeostatic controller. Due to the adaptive ability that compensates the disturbance from the water currents, the homeostatic controller was able to achieve the desired pitch angle at the fastest settling time, with an average value of 49 seconds for the whole duration. On the other hand, the MPC had the slowest settling time, with an average value of 61.5 seconds. Tables 2 and 3 summarize the controller performance results over the pitch angle. In terms of roll and yaw angle, all the controllers were able to converge to 0. However, for the roll angle, the homeostatic controller produced the shortest oscillation compared with other controllers, whereas the LQR controller had the highest glitch, and the MPC showed the longest oscillation with the lowest glitch. For the yaw angle, the homeostatic controller produced the shortest glitch and oscillation, whereas the LQR controller was associated with the highest glitch and oscillation.

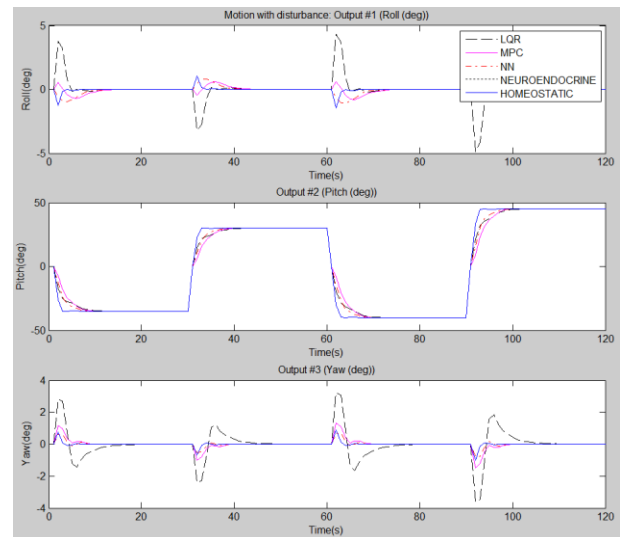


Figure 7 Comparison of the controllers' performance on Euler angles

Table 1 Desired outputs for the comparison

Simulation		Straight Gliding			
Time		30s	30s	30s	30s
Desired Angles	ϕ_d (deg)	0	0	0	0
	θ_d (deg)	-35°	30°	-40°	45°
	ψ_d (deg)	0	0	0	0

Table 2 Actual pitch angle achieved by the controller

Controller \ Pitch angle	Desired pitch angle (deg)			
	-35°	30°	-40°	45°
LQR	-35.04	30.04	-40.05	45.06
MPC	-35.09	30.08	-40.07	45.08
Neural Network	-35.04	30.03	-40.05	45.01
Neuroendocrine	-35.06	30.06	-40.07	45.08
Homeostatic	-35.06	30.06	-40.08	45.09

Table 3 Settling time for pitch angle

Controller \ Time	Settling Time (s)				
	0-30s	31-60s	61-90s	91-120s	Average
LQR	13	43	73	103	58
MPC	16	46	77	107	61.5
Neural Network	10	41	71	100	55.5
Neuroendocrine	8	37	68	98	52.75
Homeostatic	4	34	64	94	49

Figure 8 shows the comparison of the response for the controllers over the position and forces of the sliding mass, and the mass of the ballast pump. The differences of response over the r_{pz} , P_{px} and m_b among controllers were considered small. According to the analysis of the sliding mass position in the x-direction, r_{px} , the homeostatic controller produced better control performance among the controllers

because of the optimization process by the CSA in the AIS. In order to achieve the desired pitch angle, the MPC produced the longest distance of r_{px} , which was determined as 0.53 m, -0.5 m, 0.56 m, and -0.7 m. On the other hand, homeostatic controller produced shorter r_{px} than the MPC, which was determined as 0.3 m, -0.26 m, 0.35 m, and -0.39 m. This observation shows that the required distance of the sliding mass in order to achieve the desired pitch angle was shortened with a percentage value of 55.4%, 63.2%, 46.2%, and 56.9%, respectively. The neural network controller produced the shortest r_{px} .

In terms of ballast mass, the MPC produced the highest ballast mass, whereas the neural network controller produced the lowest ballast mass. The ballast mass responses of the neuroendocrine and homeostatic controllers were somewhat similar. Table 4 shows the position of sliding mass in the x-direction, r_{px} , for all controllers, and Table 5 shows the controller response over the ballast mass.

Table 4 Comparison of the position of the sliding mass in the x-direction

Controller \ Time	r_{px} (m)			
	0-30s	31-60s	61-90s	91-120s
LQR	0.52	-0.44	0.54	-0.66
MPC	0.53	-0.5	0.56	-0.7
Neural Network	0.07	-0.06	0.08	-0.09
Neuroendocrine	0.32	-0.27	0.37	-0.40
Homeostatic	0.30	-0.26	0.35	-0.39

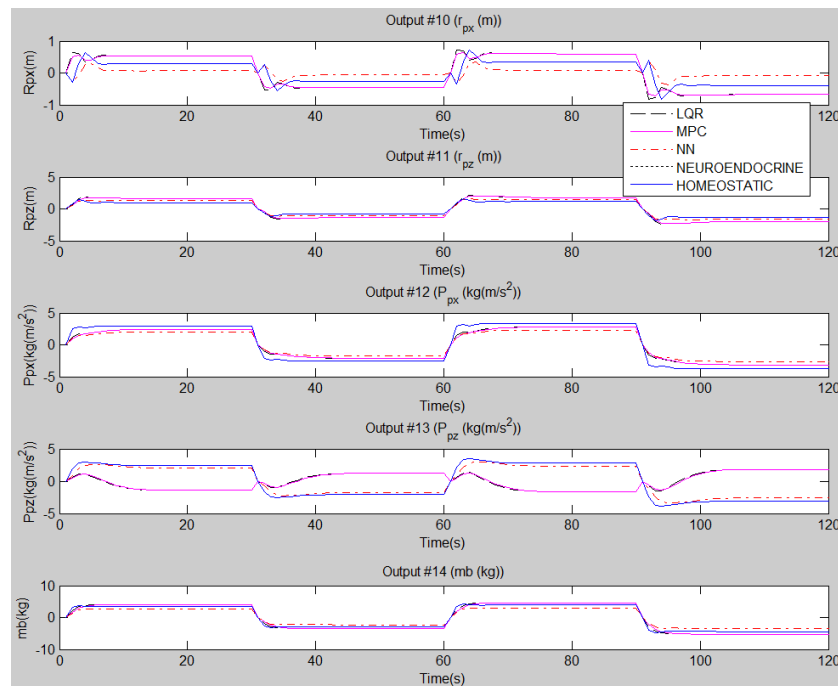


Figure 8 Comparison of the controllers performance on the sliding mass positions and forces, and the ballast mass

Table 5 Comparison of the ballast mass

Controller Time	m_p (kg)			
	0-30s	31-60s	61-90s	91-120s
LQR	4.06	-3.48	4.64	-5.22
MPC	4.07	-3.48	4.65	-5.23
Neural Network	2.66	-2.28	3.04	-3.43
Neuroendocrine	3.43	-2.94	3.92	-4.41
Homeostatic	3.40	-2.92	3.90	-4.40

4.2 Open-loop Test

In the open-loop test, the homeostatic control system was not executed since no desired outputs were specified. All of the sensor data, including the GPS data, were logged into the data logger. In this test, the internal sliding mass, ballast pump, and propeller were activated, whereas the wings and rudder were fixed straight. Figure 9 shows the open-loop system test of the hybrid-driven mode. Figures 10 to 13 show the analyses of the experimental data from the open-loop system test of the hybrid-driven mode. Figure 10 presents the Euler angles of the glider, which were taken by the IMU. During this mode, the glider had a maximum roll angle of 36.03° and a minimum roll angle of -41.89°. Furthermore, the mean and standard deviation of the roll angle were determined as 0.5° and 13.69°, respectively. The glider had a maximum pitch angle of 4.71° and a minimum pitch angle of -67.25°. In terms of mean and standard deviation, the pitch angle spread out over a wide range of values due to the gliding motion. The mean value of pitch angle was -18.8° and the standard deviation was 19.63°. For the yaw angle, the glider had a maximum yaw angle of 286.2° and minimum yaw angle of 5.7° with a mean pitch angle of 136.37° and standard deviation of 102.78°.

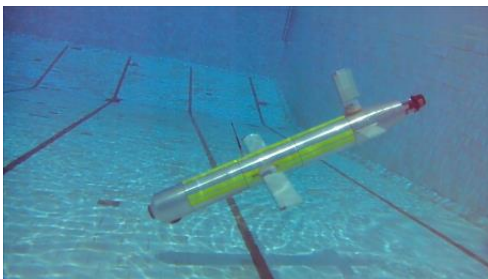


Figure 9 Open-loop system test of the hybrid-driven mode

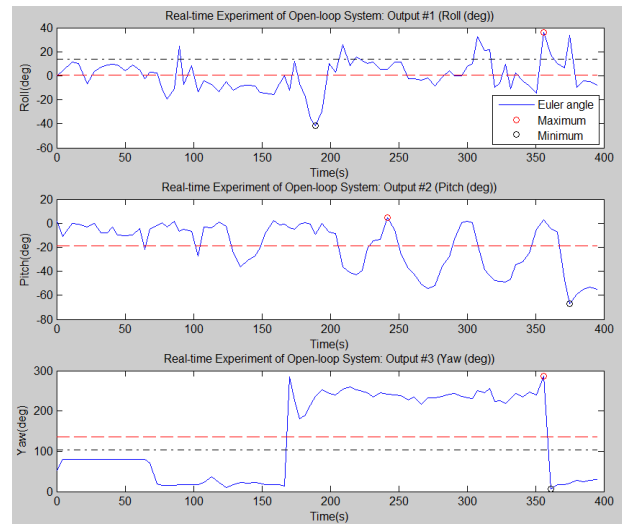


Figure 10 Euler angles of the open-loop system

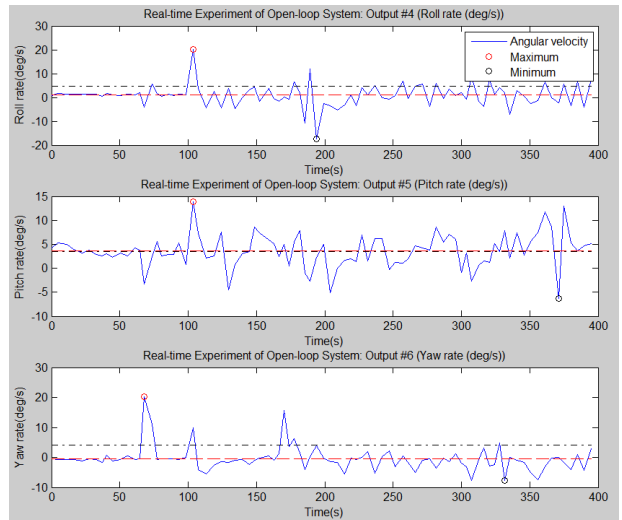


Figure 11 Angular velocities of the open-loop system

Figure 11 shows the angular velocities during the open-loop system test of the hybrid-driven mode. The glider had a minimum roll rate of -17.33 deg/s and maximum roll rate of 20.04 deg/s. Furthermore, the glider had a low mean and standard deviation, where these values were determined to be 0.99 deg/s and 4.7 deg/s, respectively. For the pitch rate, the glider had a minimum and maximum pitch rate of -6.26 deg/s and 13.92 deg/s, respectively. In terms of mean and standard deviation of the pitch rate, the value was determined to be 3.63 deg/s and 3.53 deg/s, respectively. On the other hand, the maximum yaw rate of the glider was 20.32 deg/s and the minimum yaw rate was -7.8 deg/s. Furthermore, the mean of the yaw rate was -0.38 deg/s and the standard deviation was 4.18 deg/s.

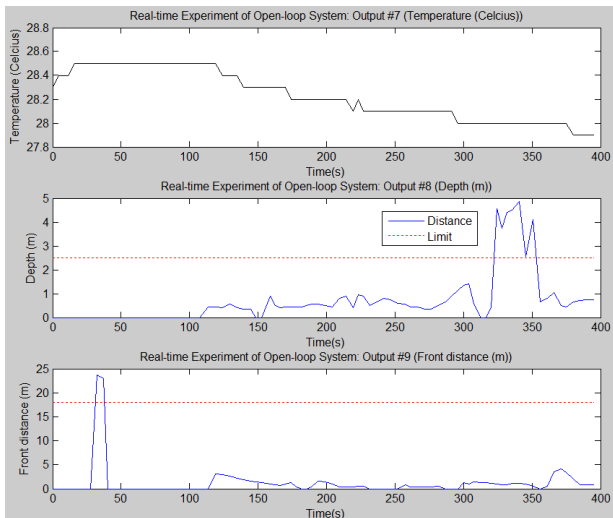


Figure 12 Real-time temperature, depth, and front distance

Figure 12 shows the temperature, depth of glider and distance of glider to the pool wall, which were detected by the echo sounders. During this operation, the minimum temperature was determined to be 27.9°C and the maximum temperature was 28.5°C with a mean value of 28.2°C. In terms of depth and distance of glider, after the error correlation was performed, the maximum depth was 4.85 m and the maximum distance was 23.7 m. Since the maximum depth and length of the diving pool is 2.5 m and 18.0 m, respectively, therefore the data provided by the vertical and horizontal echo sounders were not exactly accurate because the maximum data from both echo sounders were over the specified limit.

Figure 13 shows the GPS data during the test of the hybrid-driven mode. Since most of the GPS data were redundant, only four points of GPS data were plotted on the satellite map of the USM diving pool. The latitude and longitude that were provided by the GPS module for the whole duration were determined as [5.358188° 100.307935°; 5.358198° 100.307937°; 5.358223° 100.307945°; 5.358245° 100.307951°].



Figure 13 GPS data

4.3 Closed-loop Test and Validation

The closed-loop system test was conducted to analyze the performance of the homeostatic control system when implemented on the hybrid-driven

glider. The collected data were validated by comparing them with the simulation data of the homeostatic control system. In this test, the desired pitch angle was specified as -45° and the desired roll angle was specified as 15° for 150 seconds. Figure 14 shows the real-time homeostatic control system test of the hybrid-driven mode.

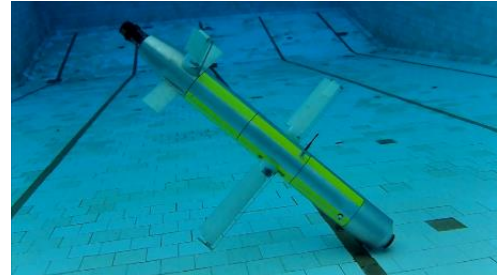


Figure 14 Closed-loop test of the hybrid-driven mode

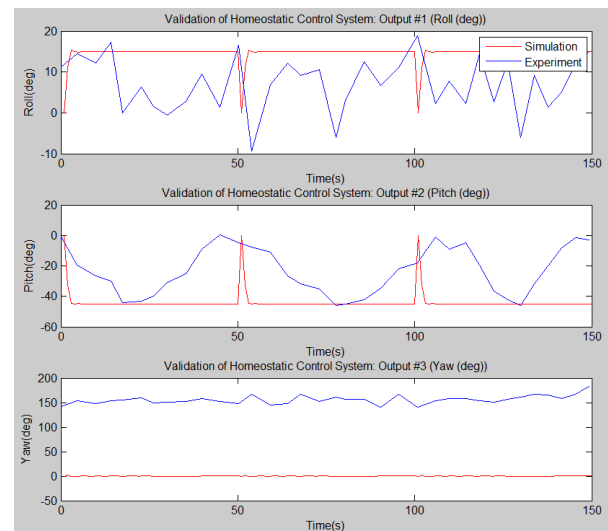


Figure 15 Euler angles of the closed-loop system

Figures 15 to 16 show the validation analysis. According to the roll graph in Figure 15, the controller did not exactly achieve the desired roll and was not able to maintain the desired roll angle. For the pitch angle, both simulation and experiment achieved the desired pitch angle. The experiment achieved a pitch angle of -44.1° for the first cycle, a pitch angle of -46.03° for the second cycle and a pitch angle of -46.03° for the third cycle. Furthermore, the settling time for the simulation was faster than in the experiment, but the controller was considered able to glide downward and upward within 50 seconds in both simulation and experiment. On the other hand, the data of yaw angle between simulation and experiment were very different.

Figure 16 shows the angular velocities during the homeostatic control system test of the hybrid-driven mode. The angular velocities of the glider during the experiment fluctuated. Similar to the buoyancy-driven mode, the roll rate for the simulation was smaller than for the experiment. The roll rate in the experiment fluctuated between a maximum value of

5.99° and a minimum value of -5.01°. The pitch and yaw rate for the simulation and experimental results were very different. The experimental results produced lower pitch and yaw rates than the simulation. The maximum and minimum pitch rates for the experiment were determined to be 17.89° and -8.21°, respectively. On the other hand, the maximum and minimum pitch rates for the simulation were determined to be 0° and -96.7°, respectively. For the yaw rate, the experiment produced fluctuating yaw rates between the maximum value of 10.79° and minimum value of -13.08°.

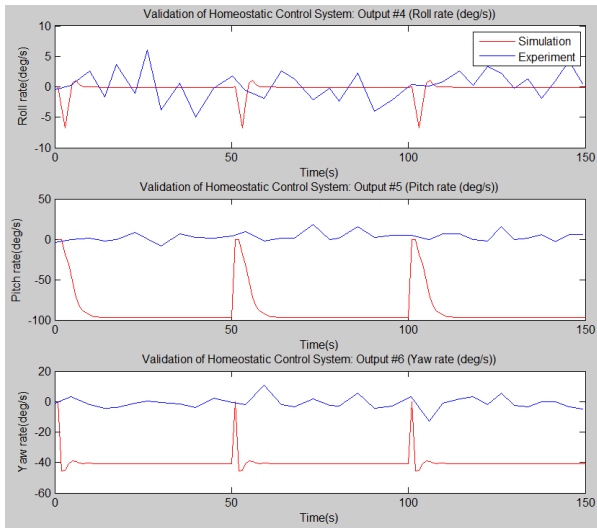


Figure 16 Angular velocities of the closed-loop system

Figure 17 shows the temperature, depth and distance of glider to the pool wall that were detected by the echo sounders. The front distance graph demonstrates that one wrong measurement occurred because the distance was over the specified limit. On the other hand, Figure 18 shows the GPS data during the homeostatic control experiment of the hybrid-driven glider. Most of the GPS data were redundant but all of them were located inside the diving pool.

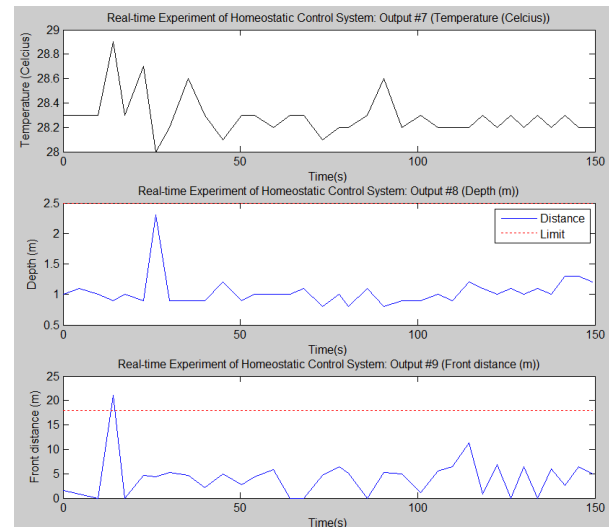


Figure 17 Real-time temperature, depth and front distance from the closed-loop system

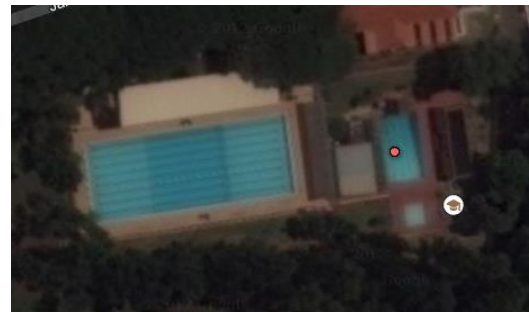


Figure 18 Real-time GPS data from the closed-loop system

5.0 CONCLUSIONS

In conclusion, this paper presents the homeostatic controller algorithm for the USM hybrid-driven underwater glider. The homeostatic controller algorithm was developed by integrating three primary systems in the human body that control homeostasis: the nervous system, endocrine system, and immune system. These three systems have been designed artificially as the ANN, AES, and AIS. The ANN was used as the backbone of the homeostatic controller, AES as the weight tuner, and AIS as the optimizer. The analyses of these three systems have been presented extensively in order to support the analysis of the homeostatic motion control system.

According to our simulation results of the control methods benchmarking, the homeostatic controller achieved the desired pitch angle at the fastest settling time, which was 12.5 seconds faster than the model predictive control (MPC), 9 seconds faster than the linear-quadratic regulator (LQR), 6.5 seconds faster than the neural network (NN) controller, and 3.75 seconds faster than the neuroendocrine controller. In addition, the homeostatic controller optimized the distance of sliding mass and ballast mass in order to achieve the desired pitch angle by shortening the sliding mass distance up to 53.7% and reducing the ballast mass

up to 17.7% when compared with the LQR and MPC. Overall, the homeostatic controller produced the best performance compared with the LQR, MPC, NN and neuroendocrine controllers.

The real-time closed-loop system test was performed in order to analyze the performance of the homeostatic control system, and to validate its performance by comparing it with simulation results. According to the validation analysis, the simulation results were more stable, linear and able to achieve the desired outputs than the experimental results. The experimental data were unstable due to the nonlinearity of the glider structure, dynamics, and real environment of the testing site that affected the sensor data. Although the homeostatic controller performance in the experiment was not as good as its performance in simulation, the results were considered acceptable and satisfactory because the controller able to achieve the desired angle.

Based on the results and conclusions of this work, several recommendations for future work could be made in order to improve the findings of this research works. In the future, the performance of the homeostatic controller will be simulated and experimentally validated on the nonlinearised glider model. It is also recommended that further research be undertaken in the areas of homeostatic controller algorithms as well as in the design of hybrid-driven AUGs. For the homeostatic controller, instead of using the feedforward neural networks or MLP as the backbone of the controller, the performance of the homeostatic could be improved by using different kinds of neural network architectures, such as recurrent neural networks or spiking neural networks. In addition, a comparison and analysis of the homeostatic controller's performance among the different kinds of neural network architectures also can be made. For the glider design, in terms of the internal sliding mass, the length of the internal actuator of the sliding mass should be longer in order to produce more forward force, as well as to produce stable and better gliding motion. In addition, a faster linear motor should be used in order to make the sliding mass move faster and to permit it to change position rapidly. By doing this, the glider would be able to glide and would achieve its desired angle faster during the buoyancy-driven or hybrid-driven modes.

Acknowledgement

The author would like to thank Malaysia Ministry of Higher Education (MOHE) ERGS-203/PELECT/6730045, Universiti Sains Malaysia (USM) and Universiti Tun Hussein Onn Malaysia (UTHM) for supporting the research.

References

- [1] Webb, D. C., Simonetti, P. J. and Jones. C. P. 2001. SLOCUM: An Underwater Glider Propelled by Environment Energy. *IEEE Journal of Oceanic Engineering*. 26(4): 447-452.
- [2] Sherman, J. Davis, R. E. Owens W. B. and Valdes. J. The Autonomous Underwater Glider "Spray". *IEEE Journal of Oceanic Engineering*. 26(4): 437-446.
- [3] Eriksen, C. C. Osse, T. J. Light, R. D. Wen, T. Lehman, T. W. Sabin, P. L. Ballard, J. W. and Chiodi. A. M. 2001. Seaglider: A Long Range Autonomous Underwater Vehicle for Oceanographic Research. *IEEE Journal of Oceanic Engineering*. 26(4): 424-436.
- [4] Osse, T. J. and Eriksen. C. C. 2007. The Deepglider: A Full Ocean Depth Glider for Oceanographic Research. *In Oceans 2007*. 1-12.
- [5] Stommel, H. The Slocum Mission. *In Oceanography*. 2: 22-25.
- [6] Bachmayer, R. Graver, J. G. Leonard. N. E. 2003. Glider Control: A Close Look Into the Current Glider Controller Structure and Future Developments. *In Oceans 2003*. 951-954.
- [7] Seo, D. C. Jo, G. Choi. H. S. 2008. Pitching control Simulations of an Underwater Glider Using CFD Analysis. *In Oceans 2008*. 1-5.
- [8] Mahmoudian, N. Woolsey. C. 2008. Underwater Glider Motion Control. *In 47th IEEE Conference on Decision and Control*. 552-557.
- [9] Leonard, N. E. Graver J. G. 2001. Model Based Feedback Control of Autonomous Underwater Gliders. *IEEE Journal of Oceanic Engineering*. 26(4): 633-645.
- [10] Lei, K. Yuwen, Z. Hui, Y. Zhikun. C. 2008. MATLAB-based Simulation of Buoyancy-driven Underwater Glider Motion. *Journal Ocean University of China*. 7(1): 133-188.
- [11] Wang, Y. Zhang, H. Wang. S. 2009. Trajectory Control Strategies for the Underwater Glider. *In Int. Conference on Measuring Technology and Mechatronics Automation*. 918-921.
- [12] Jun, B. H. Park, J. Y. Lee, F. Y. Lee, P. M. Lee, C. M. Kim, K. Lim, Y. K. Oh. J. H. 2009. Development of the AUV 'ISIM' and Free Running Test in an Ocean Engineering Basin. *Journal of Ocean Engineering*. 36(1): 2-14.
- [13] Yang, H. Ma. J. 2010. Sliding Mode Tracking Control of an Autonomous Underwater Glider. *In International Conference on Computer Application and System Modeling (ICCA SM 2010)*. 555-558.
- [14] Amin, R. Khayyat, A. A. Osgouie, K. G. 2010. Neural Networks Modeling of Autonomous Underwater Vehicle. *In 2010 IEEE/ASME International Conference on Mechatronics and Embedded Systems and Applications (MESA)*. 14-19.
- [15] Budiyo. A. 2009. Advances in Unmanned Underwater Vehicles Technologies: Modeling, Control and Guidance Perspectives. *Indian Journal of Geo-Marine Sciences*. 38(3): 282-295.
- [16] Yuh. J. 2000. Design and Control of Autonomous Underwater Robots: A Survey. *Autonomous Robots*. 8(1): 7-24.
- [17] Moioli, R. C. Vargas, P. A. Zuben, F. J. V. Husbands. P. 2008. Evolving an Artificial Homeostatic System. *In SBIA Joint Conference (SBIA)*. 278-88.
- [18] Moioli, R. C. Vargas, P. A. Zuben, F. J. V. Husbands. P. 2008. Towards The Evolution of an Artificial Homeostatic System. *In IEEE Congress on Evolutionary Computation (CEC)*. 4024-31.
- [19] Isa, K. Arshad, M. R. Ishak. S. 2014. A Hybrid-driven Underwater Glider Model, Hydrodynamics Estimation, and an Analysis of the Motion Control. *Ocean Engineering*. 81(0): 111-129.
- [20] Ezequiel A. Di Paolo. 2000. Homeostatic Adaptation to Inversion of the Visual Field and Other Sensorimotor Disruptions. *In From Animals to Animals: Proceedings of the*

- 6th International Conference on the Simulation of Adaptive Behavior. 440-449.
- [21] Hoinville, T., Henaff, P. 2004. Comparative Study of Two Homeostatic Mechanisms in Evolved Neural Controllers for Legged Locomotion. In Proceedings of IEEE/RSJ International Conference on Intelligent Robots and Systems (IROS 2004). 2624-2629.
- [22] Vargas, P., Moiola, R., de Castro, L. N., Timmis, J., Neal, M., Von Zuben, F. J. 2005. Artificial Homeostatic System: A Novel Approach. In M. S. Capcarrere, A. A. Freitas, P. J. Bentley, C. G. Johnson, J. Timmis (Eds.). Proceedings of Advances in Artificial Life. 3630: 754-764.
- [23] Moiola, R. C., Vargas, P. A., Von Zuben, F. J., Husbands, P. 2008. Evolving an Artificial Homeostatic System. In G. Zaverucha & A. LoureiroDaCosta (Eds.). *Advances in Artificial Intelligence-Sbia 2008, Proceedings*. 278-288.
- [24] Moiola, R. C., Vargas, P. A., Von Zuben, F. J., & Husbands, P. 2008. Towards the Evolution of an Artificial Homeostatic System. In *IEEE Congress on Evolutionary Computation (CEC 2008)*. *IEEE World Congress on Computational Intelligence*. 4023-4030.
- [25] Neal, M., Timmis, J. 2003. Timidity: A Useful Mechanism for Robot Control? *Informatica*. 27(4): 197-204.
- [26] Timmis, J., Neal, M., Thorniley, J. 2009. An Adaptive Neuro-Endocrine System for Robotic Systems. In *IEEE Workshop on Robotic Intelligence in Informationally Structured Space (RIISS '09)*. 129-136.
- [27] Soloway, D., Haley, P. J. 1996. Neural generalized predictive control. In *Proceedings of the 1996 IEEE International Symposium on Intelligent Control*. 277-282.
- [28] Budiyo, A. 2011. Model Predictive Control for Autonomous Underwater Vehicle. *Indian Journal of Geomarine Sciences*. 40(2): 191-199.
- [29] Timmis, J., Neal, M., Thorniley, J. 2009. An Adaptive Neuro-Endocrine System for Robotic System. In *IEEE Workshop on Robotic Intelligence in Informationally Structured Space*, part of *IEEE Workshops on Computational Intelligence*. 129-136.
- [30] De Castro, L. N., Von Zuben, F. J. 2000. The Clonal Selection Algorithm with Engineering Applications. In *Proceedings of GECCO*. 36-42.